



A preliminary research on V/N–TiO₂ self-cleaning thin film by sol–gel method under the guidance of first principle method density functional theory (DFT)

MaoMeng Wu^a, Hao Yu^{a,*}, Meng Xu^b

^a School of Materials Science and Engineering, University of Science & Technology Beijing, 30 Xueyuan Road, Haidian District, Beijing 100083, PR China

^b Powder Metallurgy Research Institute, University of Science & Technology Beijing, 30 Xueyuan Road, Haidian District, Beijing 100083, PR China

ARTICLE INFO

Article history:

Received 5 June 2012

Received in revised form

11 September 2012

Accepted 19 September 2012

Available online 5 October 2012

Keywords:

DFT

V/N-doping

Impurity band

AFM

Photocatalysis

Photohydrophilicity

Self-cleaning

ABSTRACT

A series of Ti_{1-x}V_xO_{2-y}N_y self-cleaning thin films, which can be activated driven by visible-light (VL), have been successfully immobilized on quartz glasses by sol–gel and dip-coating methods. The First Principle Method acts as guidance and reference for getting the critical (up-limitation) vanadium doping quantity in accordance with the binding energy change. Results of the band structure calculations and the doped density of states (DOS) reveal that localized impurity bands obviously existed in the band gap of TiO₂ when the V doping quantity was ca.6 at%, this film possesses the optimal visible light absorption by facilitating the transition of electron from the localized impurity band to the conduction band. Anatase crystalline phase was detected by the characterization of X-ray diffraction (XRD). TG/DTA, AFM, XPS, UV–vis, MB degradation and surface contact angle (CA) tests were also conducted for the film structural and optical properties. It is found that the mean square root (RMS) roughness of Ti_{0.94}V_{0.06}O_{1.94}N_{0.06} (13.9 nm) is ca.33 times than the others, the V, N mono-doping can increase visible light absorption (403 nm), while V/N co-doping can greatly enhance absorption in lower frequency visible region (496 nm). The MB degradation rate of Ti_{0.94}V_{0.06}O_{1.94}N_{0.06} is $7.7 \times 10^{-3} \text{ mol L}^{-1} \text{ min}^{-1}$, while the rates of N-doped and pure TiO₂ film were $(1.94 \times 10^{-3} \text{ mol L}^{-1} \text{ min}^{-1})$ ($0.8 \times 10^{-3} \text{ mol L}^{-1} \text{ min}^{-1}$), respectively. The CA on this kind of film can approach to ca. 5°. All these results indicated that the Ti_{1-x}V_xO_{1.94}N_{0.06} does well in photocatalysis and photohydrophilicity within the region of visible light. It would be a promising practical self-cleaning function and application.

© 2012 Elsevier B.V. All rights reserved.

1. Introduction

Titanium dioxide (TiO₂) has been used in a variety of forms and structures in recent decades with its unique nature properties, the wide range of engineering applications such as solar cells, photo catalysts, photochemical sensors, and functional films, etc. [1]. Among these, a self-cleaning property of anatase-type has attracted much attention, which can be caused by the synergic effect of catalysis and hydrophilicity, which as was reported by A. Fujishima and Honda in 1972 [2], R. Wang and co-workers [3–6], respectively. However, TiO₂ is a semiconductor with $E_g = 3.2 \text{ eV}$, which means that only the photo illumination energy is equal to or upward than this band gap. There is possibility that the photo-generated electron–hole pairs can be yielded, i.e. the irradiation light with $\lambda \leq 387.5 \text{ nm}$, $h\nu \geq 3.2 \text{ eV}$, which exists only in the UV wavelength region (its quantity is approximately 5% in solar energy). With respect to this low light utilization efficiency, lots of efforts have been made to make it photocatalytically and hydrophilic functional

in the visible region for different applications, such as (a) elements or ion of non-metal, such as N [7,8], F [9], B–N [10], F–N, [11], C–F–N [12] and metal, Al³⁺ [13], Fe [14], Fe³⁺/Nb⁵⁺ [15], V [16,17], and N–V [18], has been doped or co-doped. (b) Different semiconductors are coupled with TiO₂, such as WO₃ [19–21], V₂O₅ [22], PdO [23], SiO₂ [24–26]. (c) Noble metal deposition Ag [27]. (d) Surface treatment or modification, rare gas ion beam irradiation [28], corona treatment technique [29]. (e) Rare earth element Ce [30], Eu [31], etc. Almost all kinds of dopants which has been mentioned above are introduced under the guiding ideology that these introduced species (a) act as h⁺/e[−] traps, thus reducing the recombination rate and enhancing the photocatalytic and hydrophilic properties [15], (b) impurity or mid-gap states are formed, thus narrowing the band gap, which means the electrons can be excited further easily compared to pure TiO₂ with the decreased width from valence band (VB) to conduction band (CB) [32,33]. However, it also noted that the doped ions can also act as recombination centers by bouncing the h⁺/e[−] pairs or the excited electrons to valence band (VB) from intra-states when doping concentration is beyond a critical quantity based on practical experiments [15,34]. Hence, in order to obtain the expected optimal photo-responded effects, some guided theories are needed to predict the doping species and their extreme doping amounts.

* Corresponding author.

E-mail address: yhzhmr@126.com (H. Yu).

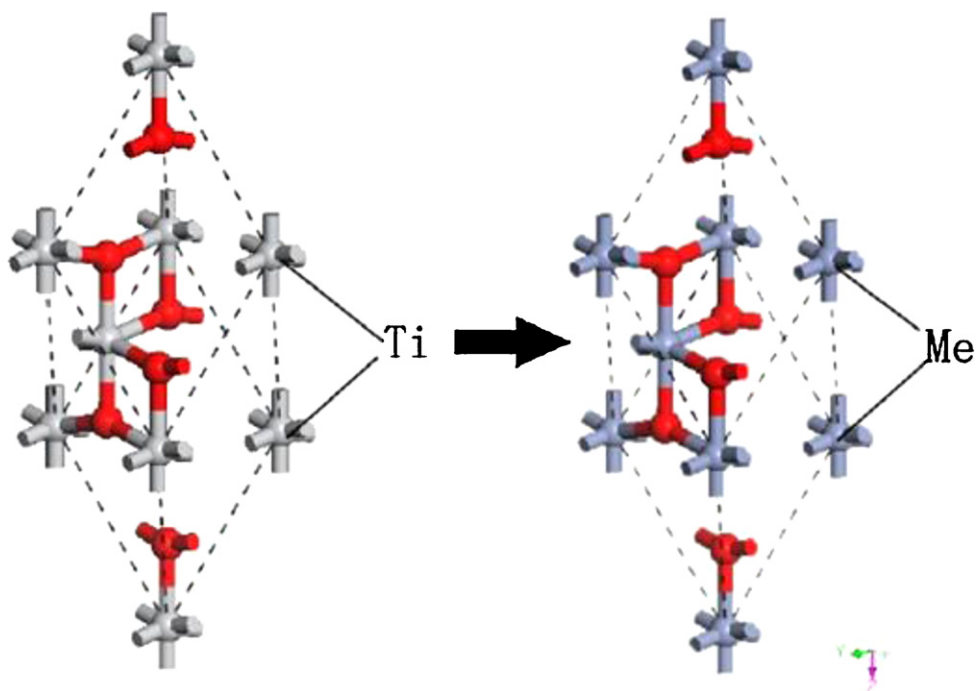


Fig. 2.1. The scheme of Ti ions was total substituted by other kinds of doped metal ions in primitive cell.

TiO₂ particles are used in application like water purification. But using immobilized TiO₂ in the form of a thin film or coating on glass, organic polymer, ceramic and metal, is more universal [35]. A variety of film preparation techniques, by far, have been applied. Such as CVD [36], magnetron sputtering [37], pulsed laser deposition [38], solvothermal method [39], and sol–gel method [14,15,22,24], etc. Among these methods, sol–gel is a frequently used wet-chemistry process to get thin film with nano-sized and equipments simplicity, the pinpoint reagent ratio, high degree of homogeneity and low reaction temperature, etc. Hence, this technique could be an appropriate method for the preparation of self-cleaning film.

Although a great number of works have been done about N and V doping, little is done to quantify whether effective red-shift of thin film prepared from the co-doped TiO₂ sols has been caused, and there lacks the theoretical characterization for doping effects on host electronic and optical properties. Therefore, in this article, we first predict the band energy changes of N and V co-doped TiO₂ by DFT plane-wave pseudo-potential method [40] using the program CASTEP 5.0 [41] that is launched by Accelry company. Aiming to ascertain the dopant limitation and then determine the suitable atom ratio for acquiring optimal visible-light responsibility, after corresponded to the analog computation computer simulation, the thin films with doped-TiO₂ sol are prepared by sol–gel and dip-coating method to verify the above theory calculation.

2. Theoretical calculations

2.1. The dopant up-limitation

In this stage of research, the lattice parameters of anatase TiO₂ are $a = b = 3.812 \text{ \AA}$ and $c = 9.478 \text{ \AA}$, a primitive cell with 6 atoms (containing 2 Ti and 4 O atoms, respectively) being used as model (see Fig. 2.1). The doped limitation of transition metal V ion can be basically determined through the empirical equation $M = -\Delta E/2$, while

the binding-energy before and after doping are figured out by the following formula:

$$E_b(\text{Ti}) = 2E_{\text{Ti}} + 4E_{\text{O}} - E_f \quad (2-1)$$

$$E_b(\text{Me}) = 2E_{\text{Me}} + 4E_{\text{O}} - E_f \quad (2-2)$$

where E_{O} , E_{Ti} , E_{Me} , E_f represent the free energy of the oxygen, titanium, metal atoms and the final energy of primitive cell, respectively. So ΔE was easily known from the quantity difference between $E_b(\text{Ti})$ and $E_b(\text{Me})$, and then, the dopant up-limitation (x), is determined by the following condition and equation:

$$M \geq 0, x = 100\% \quad (2-3)$$

$$M > -15\% \times \frac{E_b}{2}, x = e^{0.05 \times M \times 49} \quad (2-4)$$

$$M \leq -15\% \times \frac{E_b}{2}, x = \frac{1}{1 - (M \times 49)} \quad (2-5)$$

On the basis of the above ΔE , the doped elements up-limitation (at%) of IVB transitional metal are all enumerated, which is in accordance with the conclusion of Qu et. al. [42] (see Table 2-1). According to the simulation, we choose a series of V concentration (0–6 at%) to dope the TiO₂, and the density of states (DOS) of the representative film is obtained by simulation to verify the change of band state.

2.2. The simulate calculation process

The doping simulation in anatase structure is done in this stage. The lattice parameters of anatase TiO₂ are set $a = b = 3.812 \text{ \AA}$ and $c = 9.478 \text{ \AA}$, a $2 \times 2 \times 1$ super-cell [12] with 48 atoms (containing 16 Ti atoms and 32 O atoms) is chosen as model (see Fig. 2.2). In the mono-doping ($\text{Ti}_{1-x}\text{V}_x\text{O}_2$ or $\text{TiO}_{2-y}\text{N}_y$) cases, only one V or N atom is introduced to substitute Ti or O atom in super-cell respectively. One N atom can accept one more electron than O atom and one V atom can donate one more electron than Ti atom, which means the site of substitution act as a single acceptor and donor, respectively. As a result, electrons of V and N atom are compensated, which results

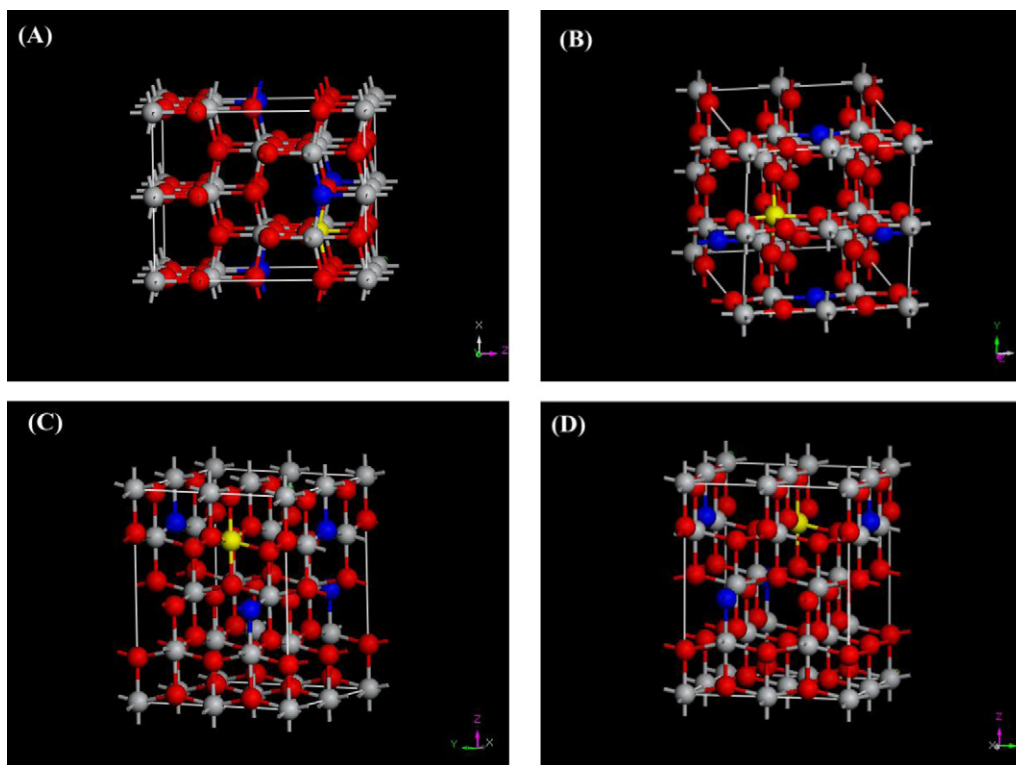


Fig. 2.2. The anatase TiO_2 $2 \times 2 \times 1$ supercell model.

in an inactivated doping in the super-cell [43]. However, it is a non-inactivated doping when substituted with one V atom and two N atoms or two V atoms and one N atom meanwhile in the super-cell.

The calculation is carried out with structure optimization coupled with the minimized total energy and ionic force. The density functional theory realized with Perdew–Burke–Ernzerh (PBE) method [44] and the generalized gradient approximation (GGA) is applied to describe exchange–correlation effects, to ensure the accuracy of the calculation, the pseudo-potential is adopted to describe electron-ion interactions with kinetic energy cutoffs of 386.5 eV, The Brillouin-zone is restricted to the Γ point in geometry optimization, the K -points grid is set to $3 \times 3 \times 3$ and $1 \times 1 \times 1$ in line with different substitute sites in energy calculations, the energetic convergence threshold for self-consistent field (SCF) is 10^{-5} eV/atom, atomic relaxation is not carried out until all components of the residual forces are less than 0.01 eV/nm and the maximum ionic displacement is within 0.001 Å in the geometry optimizations, respectively. Each atom valence in the simulation calculation is O ($2s^2 2p^4$), N ($2s^2 2p^3$), Ti ($3s^2 3p^4 3d^2 4s^2$), and V ($3s^2 3p^6 3d^3 4s^2$), respectively. The density of states (DOS) of doped TiO_2 structure is calculated in the reciprocal space.

3. Experiment

3.1. Film preparation

A series of $\text{Ti}_{1-x}\text{V}_x\text{O}_{1.94}\text{N}_{0.06}$ and $\text{Ti}_{1-x}\text{V}_x\text{O}_2$ ($x=0-0.06$) sols were synthesized by proportioning the raw material molar ratio and the following process. Firstly, pure TiO_2 sol was prepared through the controlled hydrolysis of tetra-*n*-butyl titanate (TBOT). A series of molar of tetra-*n*-butyl titanate with the corresponding quantity ($1-x$), were slowly added into two-thirds of ethanol and acetyl-acetone (as the chelating agent for Tetra-butyl titanate) mixed solution (volume ratio ca. 5:1) under the continuous stirring about 2 h, The above sol formed henceforth abbreviated as

Ti(A)-1, ~Ti(A)-4 were used to generate N or V and N/V co-doped sols respectively. Secondly, According to the doping quantity x ($x=0-0.06$), solution named V(B)-1~V(B)-4 were synthesized by mixing the Vanadyl(IV)-acetylacetone and the rest ethanol, and the nitric acid is use for adjusting pH. Then, solution V (B) is added into corresponding Ti (A) drop by drop under further 2 h of vigorous stirring at ambient temperature 30°C . The color of sols change from bright yellow to bottle green gradually and finally invisible green with the increasing V molar quantity, after continuous stirring for 4 h, V-doped TiO_2 sol was obtained. Thirdly, urea (6×10^{-3} mol) was dissolved into the de-ionized water (0.6 mol) and ethanol (0.6 mol) with stirring 0.5 h to obtain the solution N(C). The as-prepared N/V co-doped TiO_2 sols can be obtained after adding the N(C) into the above mixed (A+B) sol.

Here, the doped amount of the nitrogen is 6 at% while altering the vanadium doped concentration. We refer to the conclusions that are derived from Liu et al. [43] and Kitano et al. [45]. The calculations in literature of Liu show that the relative optimal N-doped concentration is ca. 6 at%. This theoretical prediction was verified by the UV–vis absorption spectra of subsequent samples. Nitrogen atoms were able to substitute oxygen in the range of 2–16.5% in Kitano's research. Such a high-level doping was not achieved

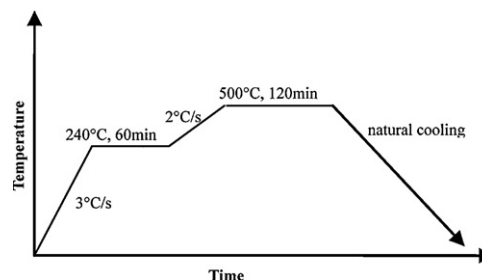


Fig. 3.1. The linear rising temperature program of post heat-treated in furnace.

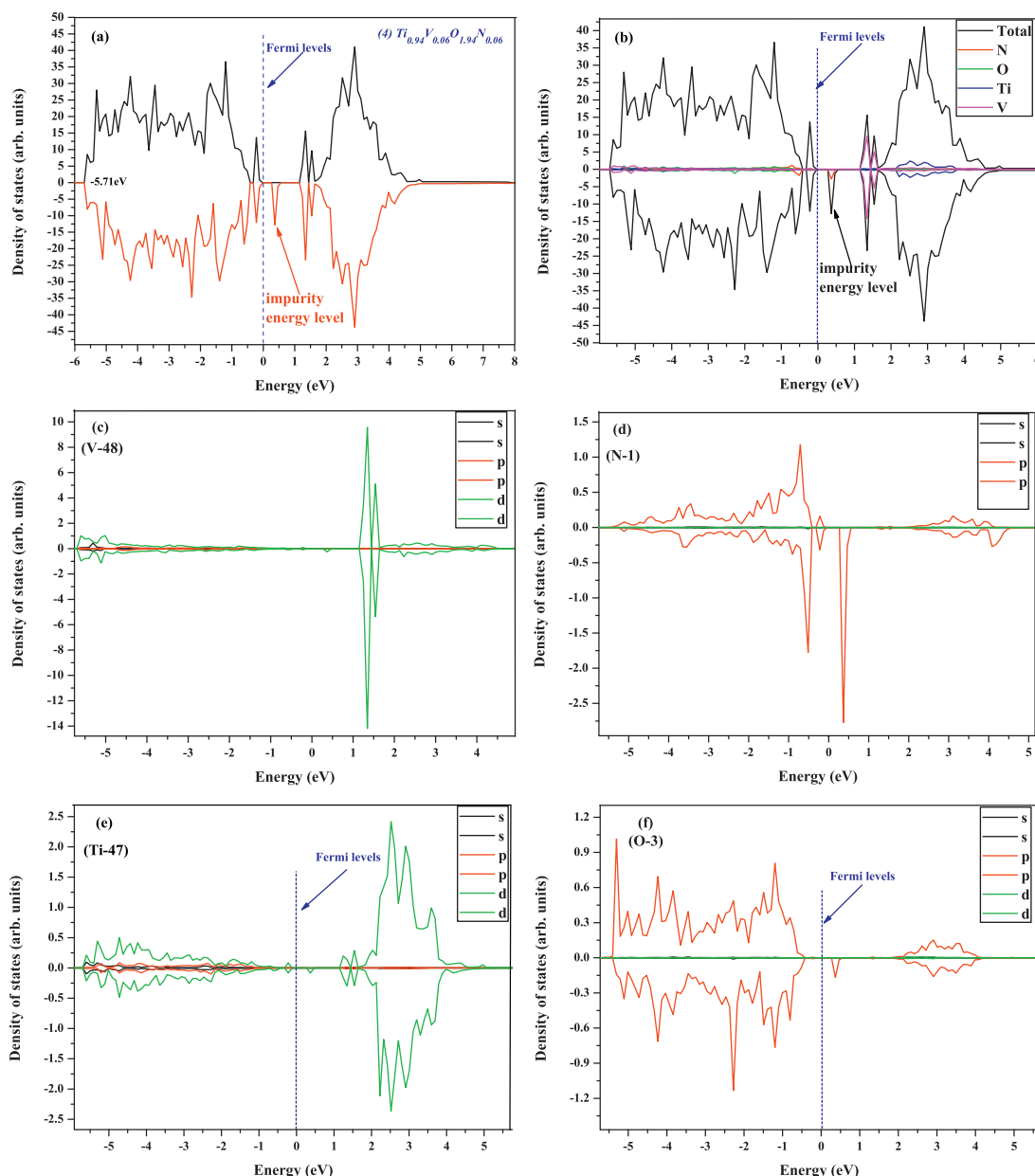


Fig. 4.1. The simulation calculation chart of the super-cell anatase TiO_2 model. (a) TDOS of (4) sample, (b) schematic contribution diagram of ilka atom, (c)–(f) were the DOS figures of V-48, N-1, Ti-47, O-3, respectively.

previously and resulted in a steep absorption edge in the visible light region [45]. A film photo-catalyst with a nitrogen concentration of 6% (strong absorption up to VL region) exhibited the highest reactivity for the photocatalytic oxidation of 2-propanol in water under visible irradiation ($\lambda > 450 \text{ nm}$). Higher nitrogen concentration would introduce large amounts of oxygen vacancies in the films and result in lower VL-activity [45].

The $40 \text{ mm} \times 20 \text{ mm} \times 1 \text{ mm}$ and $20 \text{ mm} \times 10 \text{ mm} \times 1 \text{ mm}$ quartz glass plates are used as the substrates, the substrates which are first washed in water-free ethanol, deionized water and acetyl acetone 15 mins sequentially. After stoving at 40°C in air oven, these substrates are coated with above sols with a constant withdrawal speed $\text{ca. } 1 \text{ mm s}^{-1}$, and then heat-treated in furnace with a linear rising temperature program (see Fig. 3.1). Repeat this cycle 5 times until achieve the as-prepared thickness. The films are labeled as N/Ti-0.06/1, V/Ti- $x/(1-x)$ and V/N/Ti- $x/0.06/(1-x)$, respectively.

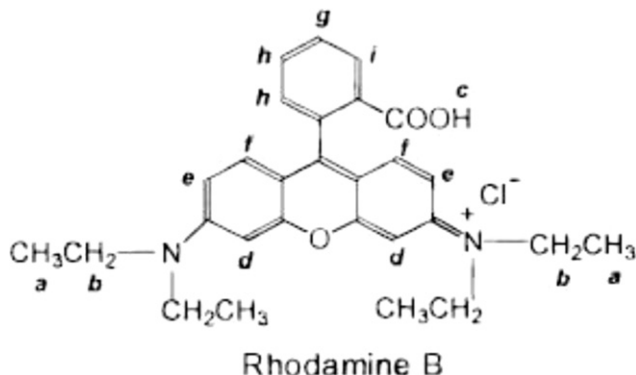
3.2. Film characterizations

In order to acquire the optimal annealing temperature program of film crystalline, the thermal properties of gel were investigated by thermal analyzer TG (WRT-3P)–DTA (WCR-2C). The crystalline of all films that post heat-treated were determined by using XRD (Rigaku DMAX-RB, XD-98 $\text{Cu K}\alpha = 1.5406 \text{ \AA}$, 40 kV and 150 mA), the crystal size of anatase spike (101) was determined by the Scherrer equation: $D_{hkl} = k\lambda/(\beta \cos \theta)$, where K is related to the crystallite shape; λ and θ are the radiation wavelength and Bragg's angle, $\beta = B_0 - b_0$, XRD was scanned a range of 2θ ($10\text{--}85^\circ$, $5^\circ/\text{min}$), 2° step size to observe the overall XRD peaks to identify the transformation of crystal phase. Top surface morphologies (2D, 3D) and mean square root roughness (RMS) of thin films were evaluated by Atomic Force Microscopy (AFM: Nano Scope 3a, Digital Instruments, Santa Barbara, CA). X-ray photoelectron spectroscopy (XPS) measurements to show the depth profile of C, N, V atoms

in the TiO₂ lattice (Shimadzu Corporation Kratos, AXIS ULTRA^{DLD}, mono-Al K_{α} = 1486.6 eV, 150 W, Vacuum degree 2×10^{-9} Torr). All the binding energies are calibrated by the C1s peak at 284.8 eV for the adventitious carbon. UV–vis absorption spectra of all films were measured by the model U-3900H Spectrophotometer (200.00–800.00 nm, 5.00 nm/s, Interval 0.50 nm, Delay 1 s).

3.3. Film self-cleaning tests

Surface wettability of films is tested with water contact angle (CA) measurement by using a Kruss DSA 100 drop shape analyzer with the waterdrop volume 2 μ L, illuminated by visible light ($\lambda \geq 420$ nm) and kept in dark for different lengths of time. Every sample is measured 6 locations to get an average value. The evaluation of the photocatalytic activity was accomplished by the degradation of Rhodamine B (RhB, C₂₈H₃₁ClN₂O₃). The initial concentration is 0.012 mM. The coated substrates were first immersed in RhB solution about 60 min for sufficient soaking in the absence of light, and then exposed to the light source ($\lambda \geq 420$ nm). The irradiation ambient temperature is 30 ± 1 °C, the RhB photo-catalytic efficiency can be converted by measuring the solution absorption spectrum peak at 551 nm on each interval of 50 min. The photocatalytic reaction is a pseudo-zero-order relation with the reaction rate constant k , where $C/C_0 = e^{-kt}$.



4. Theoretical results

From the figures that is obtained from DFT simulate calculation, the conclusion, which the impurity energy level was definitely arising between the CB (combined with V3d) and the VB (combined with N2p), can be undisputed drawn. Or rather, the impurity energy level was the combined action of V and N which can be demonstrated by several band energy and strength that is shown in the figures (b)–(d). This level can facilitate the light arousal process and the quantum efficiency, and the photo responsibility can be enhanced eventually (Fig. 4.1).

5. Results and discussion

5.1. Effects of annealing temperature on film

High annealing temperature not only removes organic impurities, which may affect the integral structure of the films, but also results in the crystallization of coated gel and crystal form transition. In order to estimate the annealing temperature influence on film and then acquire the suitable linear warning up program for film crystallization, the thermal property of (4) sample gel was investigated by thermal analyzer TG (WRT-3P)-DTA (WCR-2C).

The (4) sample gel TG-DTA thermal analysis results are shown in Fig. 5.1, which indicate that the TG curve (Fig. 5.1a) can be separated into several zones: in the 1st zone from room temperature to

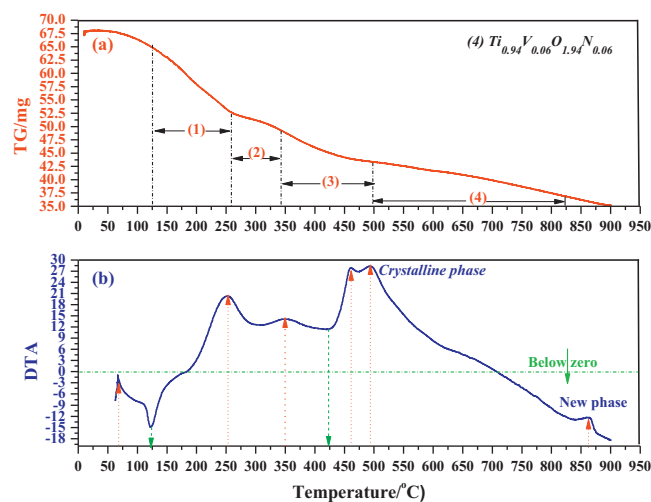


Fig. 5.1. Thermal analysis of (4th) sample ($x=6$ at%, $y=6$ at%) gel after 30 °C drying: (a) TG and (b) DTA properties.

130 °C, the weight loss is about 7%, which corresponds to the gradual endothermic process as is shown from the DTA curve (Fig. 5.1b). This zone mainly corresponds to the removal of acetyl acetone, ethyl alcohol and physically adsorbed water. In the 2nd zone from 130 °C to 252 °C, approximately 22% weight loss is mainly caused by the evaporation of urea (boiling point 235 °C) and combustion of organic/its compounds including acetyl acetone, residual other organic intermediates, which corresponds to an evident exothermic peak at 250 °C in the DTA curve. The 3rd zone (2, 3 stages of Fig. 5.1(a), 250–460 °C), was attributed to oxidation of residual chemical absorption water or the intermediate compounds from degraded urea resulting in a weight change of approximately 18%, which corresponds to an evident exothermic peak at 460 °C in DTA curve. It is worth noting that there is a small endothermic peak with the very narrow intervals between 460 °C and 500 °C, which indicates some organic groups or macromolecule absorbed on the surface of the gradual decreased crystal were removed, and that crystalline phase transition/lattice distortion or final perfect growth emerges. There is another small exothermic peak in the last zone with the temperature about 860 °C, on behalf of the crystal phase transformation to another type of titanium dioxide.

The film warming up program is designed by judging from the above thermal stage, the formation of anatase can be confirmed by XRD analysis in Section 5.2.1.

5.2. Surface structure analysis of film

5.2.1. XRD structural and N₂ adsorption analysis

The XRD diffraction patterns of nitrogen/vanadium mono- and co-doped TiO₂ films are shown in Fig. 5.2. The anatase type was manifested by its fingerprint peak of 2θ values at 25.4°, 38.1° and weakly at 48.1°, these are assigned to diffraction (hkl) plane (1 0 1), (0 0 4) and (2 0 0), respectively. Simply judging from the increasing intensity and width of (1 0 1), we can infer that there is gradual perfecting anatase crystallinity with increasing dopant quantity. The XRD profiles was carried out using the DBWS Rietveld refinement program with a Cerius-2 interface to exactly determine the crystallographic parameters of all the samples for it is an effective way to providing the quantitative structural information of crystalline materials. According to the refinement, the crystal unit cell grain sizes and lattice parameters of films are listed in Table 1a. On the one hand, it shows that the grain sizes of as-prepared N, V mono- and N/V co-doped samples are nanometer scale. However, the (1)–(4) and (1')–(4') grain sizes, which are calculated by

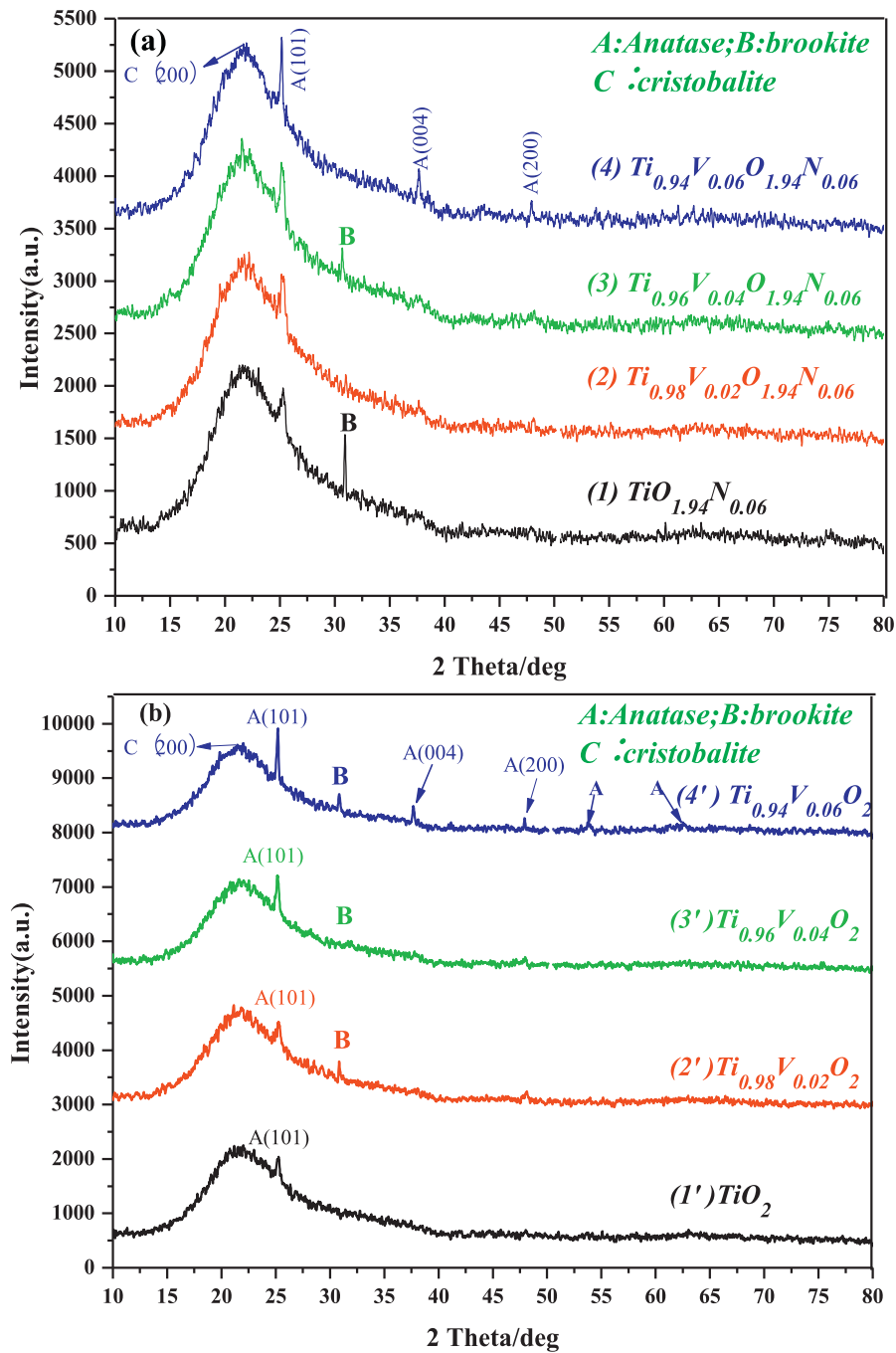


Fig. 5.2. X-ray diffraction of post heat treated films. (a) $x=0\text{--}6\text{ at\%}$; $y=6\text{ at\%}$ doping concentration, (b) $x=0\text{--}6\text{ at\%}$; none y , respectively. With the same post heat treated program.

using Scherrer equation based on the full width at half maximum (FWHM) and anatase phase spike (1 0 1), presenting a reducing (from 66.1 nm to 26.6 nm) and increasing (from 29.8 nm to 71.1 nm) tendency with the increasing x values, respectively. These results correspond with the AFM results in Section 5.2.2. This indicates that V and N species have been incorporated into the lattice of anatase TiO_2 with varying extent and V/N co-doping restrains the grain

growth more efficiently than mono- samples. Hence, a conclusion that the doping has a great influence on grain size is drawn. On the other hand, V/N co-doped TiO_2 shows a slight larger expansion of the lattice parameters along with both “ a ” and “ c ” axes compared with pure and N or V mono-doped TiO_2 . This also indicates that V and N species have been incorporated into the lattice of anatase TiO_2 with varying extent.

Table 1
The results of doped elements up-limitation (at%) of IVB transitional metal.

IVB	Sc	Ti	V	Cr	Mn	Fe	Co	Ni	Cu	Zn
Doping limitation (at%)	0.2	100	7.9	0.8	0	0.3	0.2	0.2	0.1	0.1

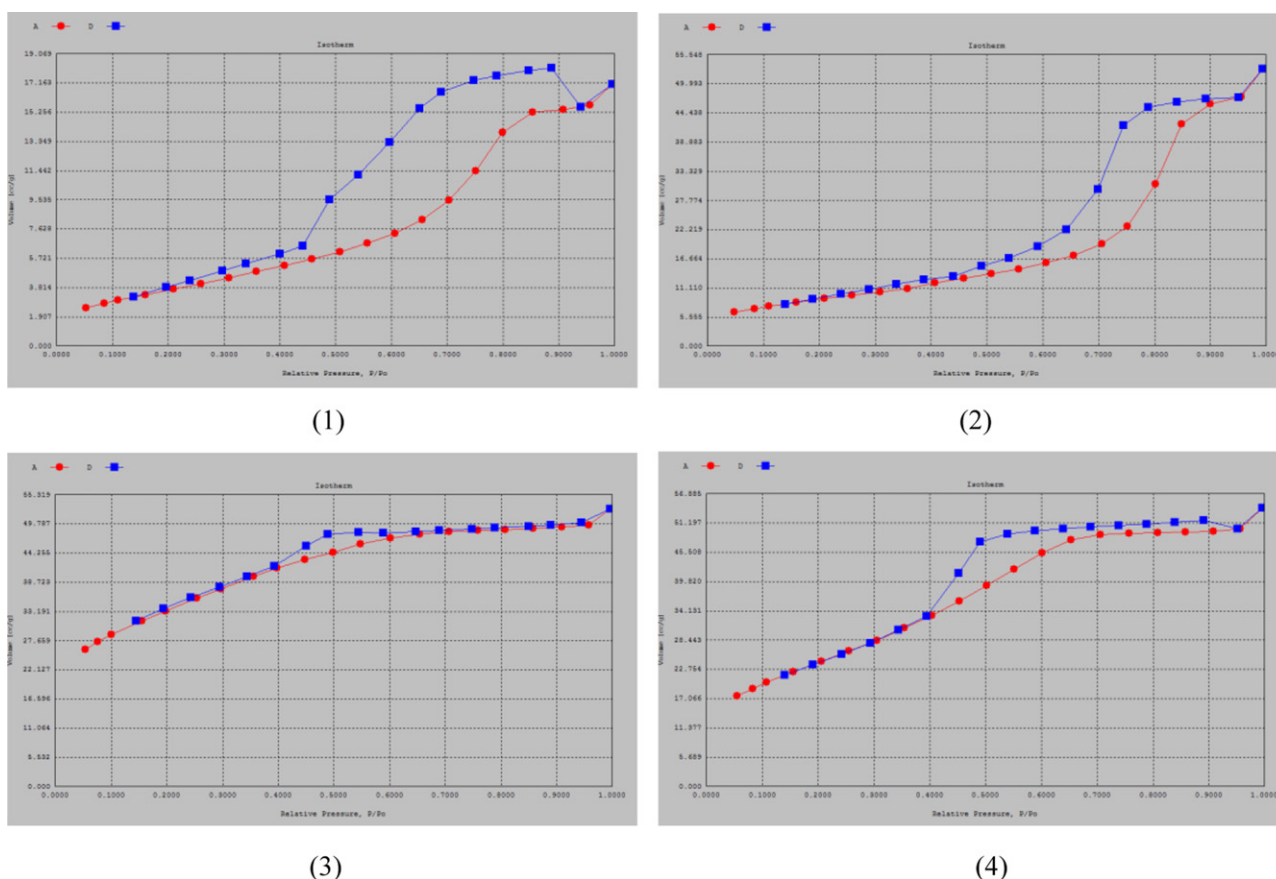


Fig. 5.3. N₂ adsorption and desorption isotherms analysis of (1), (2), (3), (4) TiO₂ thin films, respectively.

Scherrer formula:

$$D_{hkl} = \frac{k \cdot \lambda}{\beta \cdot \cos \theta} \quad (5-1)$$

where K is related to the crystallite shape (generally is 0.89); λ and θ are the radiation wavelength and Bragg's angle, and (i.e. FWHM), respectively.

There are several furthersome influences in photo responsibility for the smaller particle size. As a kind of catalyst that is acted by the redoxomorphism of photo-excited electron-hole pairs. On the one hand, peculiarities relating grain were made clear that the photocatalytic activity was enhanced with the decreased grain size owing to the enhanced redox ability which is due to the increase of E_g (energy gap). On the other hand, the photo quantization efficiency (QE) will be improved through the effective separation of electron-hole pairs, on account of the photo-induced carrier diffusion time, which is derived from diffusion equation (see formula (5-2)) from interior to surface and was curtailed due to the small grain size.

$$\tau = \frac{r}{\pi^2} \cdot \frac{1}{D} \quad (5-2)$$

where τ is the average diffusion time; r is the grain size; D is the diffusion coefficient.

On the other hand, the N₂ adsorption and desorption analysis was performed by using AUTOSORB-1 AS1Win Version 1.50 Adsorption Analyzer in order to obtain the detail information of these kinds of thin films. The results were shown in Fig. 5.3 and the pore characterizations of the film surface were exhibited in Table 2.

Fig. 5.3 reveals these samples are of type IV (BDDT classification). The hysteresis loop shape changes in link with the increasing V dopant correspondingly, which indicates an evolution of

mesoporosity in the films. There is a tendency of BET area (total adsorption as well as single point) that gradually increases first and drop to a small figure then, which means the sample (3) will have greater adsorption ability. The change of special surface did not fully meet the tendency of crystal grain size (refer to Table 2a), which may be attributed to the nature affluence of pore that exists in the films [46]. The results of the N₂ adsorption and desorption analysis reveal that the films have the surface adsorption abilities that are beneficial to the photo responsibility.

5.2.2. AFM graph analysis

Since the wettability of films was largely influenced by surface structure, a root mean square (RMS) roughness was investigated and obtained from AFM images. The RMS roughness was calculated according to the following equation:

$$RMS = \sqrt{\frac{\sum_{i=1}^N (Z_i - Z_{av})^2}{N}} \quad (5-3)$$

where Z_{av} is the average height for the entire region, Z_i is the height of individual point i , and N is the number of points measured within a given area [47].

2D topographical images are shown in Fig. 5.4A to reveal the articulated square-like crystalline grains, which was consistent with the results of T. Taguchi et al. [48] work that is shown in Fig. 5.4B, bestridden over the entire surface homogeneous and multistory (or other laminated construction). It is noted that there are few holes of unequal size existing among the crystalline grain that enlarge the specific surface area, and the crystal boundary becoming smoothed gradually and connected closely. This kind of structure is beneficial to the film surface wettability. It also can be seen that the grain sizes of the (1)–(4) films were reduced with

Table 2a

Crystal unit cell information and phase type quantity from XRD data, AFM surface roughness (RMS) for all the samples.

Sample	Lattice parameter ^a		Grain size ^b (nm)	Anatase quantity (%)	Surface roughness (nm)
	<i>a</i> (Å)	<i>c</i> (Å)			
TiO ₂	3.7848	9.5142	29.8	99%	1.32
Ti _{0.98} V _{0.02} O ₂	3.7881	9.5145	31.2	97%	1.40
Ti _{0.96} V _{0.04} O ₂	3.7890	9.5149	68.8	98%	1.56
Ti _{0.94} V _{0.06} O ₂	3.7895	9.5150	71.1	95%	12.9
TiO _{1.94} N _{0.06}	3.7889	9.5148	66.1	96%	0.414
Ti _{0.98} V _{0.02} O _{1.94} N _{0.06}	3.7991	9.5151	49.6	98%	0.766
Ti _{0.96} V _{0.04} O _{1.94} N _{0.06}	3.7994	9.5154	32.3	97%	0.958
Ti _{0.94} V _{0.06} O _{1.94} N _{0.06}	3.7996	9.5146	22.9	99%	13.9

^a Calculated from XRD by using Jade 5.0 (MDI/Rigaku) software.^b Calculated from the (1 0 1) diffraction peak of anatase using the Scherrer equation from XRD.

V doping concentration with the same N concentration, which is consistent with the XRD results of Fig. 5.4A–(d) in Section 5.2.1.

Fig. 5.4C shows the 3D images that correspond to the 2D images in Fig. 5.4A. The most valuable information we can derived from these 3D images is that the surface RMS, which is highly related to the surface hydrophilicity [8,14,22,24]. Let us take (4) film as an example, the height of protruding grain within the scanning area was ca.95 nm, which is approximately 10–12 times higher than the first three samples. The appearance of crystalline grain turns into mellow and the boundary of grain becomes more compact than other samples, which is favorable to the spreading of the water on the film surface, then the contact angle of hydrophilic surface decreases with increasing roughness provided that the surface remains identical chemistry.

Those 2D and 3D images of V mono-doped films have the similar variation tendency as compared with the series of N and V/N doped films (which are not shown here).

5.2.3. XPS analysis

XPS spectrum was used to obtain the surface compositions of V, N mono- and V/N co-doped thin TiO₂ films. Typical XPS full spectrum of (*x* = 0 at%, *y* = 6 at%), (*x* = 6 at%, *y* = 6 at%) thin film is shown in Fig. 5.5a. All samples share a common peak located at 284.8 eV, which is ascribed to the contaminant carbon in the instrument testing process with no objection. In addition, weak peaks positioned at ca. 286.1 and 288.9 eV were presented in Fig. 5.5f, and these two peaks are assigned to C=O and C–N bonds. There is also a conclusion that the N-doped quantity in (4) film outnumber that in (1), which can be drawn by referring to the ratio of the peak. These carbonaceous species incorporated could act as photo-sensitizer to induce the visible-light absorption and response, which was possibly responsible for the enhanced visible–light photo-catalytic activity [51].

The spectra of N1s are exhibited in Fig. 5.5b, two peaks and one peak for samples of (*x* = 0 at%, *y* = 6 at%) and (*x* = 6 at%, *y* = 6 at%), respectively. These three peaks show the absence of the 396 eV

(extending from 399.9 eV to 402.7 eV), which indicates that N1s has been doped into the lattice of TiO₂ for the peak around 399.9 eV is assigned to the Ti–N–O and Ti–O–N sites (interstitial N), while peaks around 400.7 eV and 402.7 eV in (4) film are assigned to O–Ti–N (substitutional N). According to the DFT calculation of sample (4), there is a mild hybrid impurity band on the top of the valance band (VB), indicates that the V/N co-doping easier induces the impurity band through the overlapping of N2p and O2p, therefore, a better visible light induced photo-catalytic activity was efficiently obtained. The other message from the graph Fig. 5.5b is that the N1s shift of (4) film is greater than that of (1) can be obtained, which might means that the existence of V may avail to decrease the energy barrier for N incorporation [18,49].

Fig. 5.5e shows the O1s peaks that exist in (1) and (4) film. The peak at ca. 529.6 eV belongs to the normal Ti–O bonds in TiO₂ lattice, while the peak at ca. 531 eV was attributed to the H–O bonds of the surface hydroxyl groups, we can also refer that the V/N co-doped samples possess relatively more hydroxyl quantity than mono-doped one, this might account for the difference of photo-induced properties among these two films.

Fig. 5.5c and d shows the V2p_{3/2}–V2p_{1/2} and V2p_{3/2} curves of (4) film which were fitted by Shirley and Lorentzian-Gaussian method, respectively. Peaks at ca. 514.7 eV and 515.8 eV in V2p_{3/2} (Fig. 5.5d) are ascribed to V³⁺ and V⁴⁺, respectively. This suggests that V species exist in the anatase lattice of V–N–TiO₂ in the form of V³⁺ and V⁴⁺ [18]. Since the proportion of nitrogen and vanadium that were incorporated with the lattices has a great influence on the properties of TiO₂ thin films, the percentage of composite elements in film were calculated and listed in Table 3.

As seen in Fig. 5.5g, the binding energy and peaks of Ti 2p are about 458.8–460.0 eV for Ti 2p_{3/2} and 463.8–464.9 eV for Ti 2p_{1/2}. The peaks at ca. 458.5 and 464.7 eV are assigned to TiO₂. While the weakly peaks, such as 458.6, 459.7, 463.8 and 464.0 eV, may be linked with the presence of various carbon, nitrogen and vanadium species, such as Ti–C, Ti–N–O, Ti–O–N, O–Ti–N and Ti–O–V bonds [51]. This is in agreement with the results as shown in Fig. 5.5(b), (e), (f), and (g).

Table 2bBET area, pore volume, pore size, liner correlation coefficient and single point of (1), (2), (3), (4) TiO₂ thin films, respectively.

Samples	BET area (m ² /g)	Pore volume (cm ³ /g) ^a	Pore size (nm) ^b	Liner correlation	Single point BET (m ² /g) ^c
TiO _{1.94} N _{0.06}	14.34	0.02627	74.77	0.9989	13.42
Ti _{0.98} V _{0.02} O _{1.94} N _{0.06}	31.64	0.08133	102.8	0.9969	30.94
Ti _{0.96} V _{0.04} O _{1.94} N _{0.06}	115.7	0.08099	28.09	0.9976	114.62
Ti _{0.94} V _{0.06} O _{1.94} N _{0.06}	89.18	0.08329	37.36	0.9996	85.90

^a Single point desorption total pore volume of pores at *P*/*P*₀ = 0.99.^b BJH adsorption average pore width.^c Single point pore volume of pore at *P*/*P*₀ = 0.3.

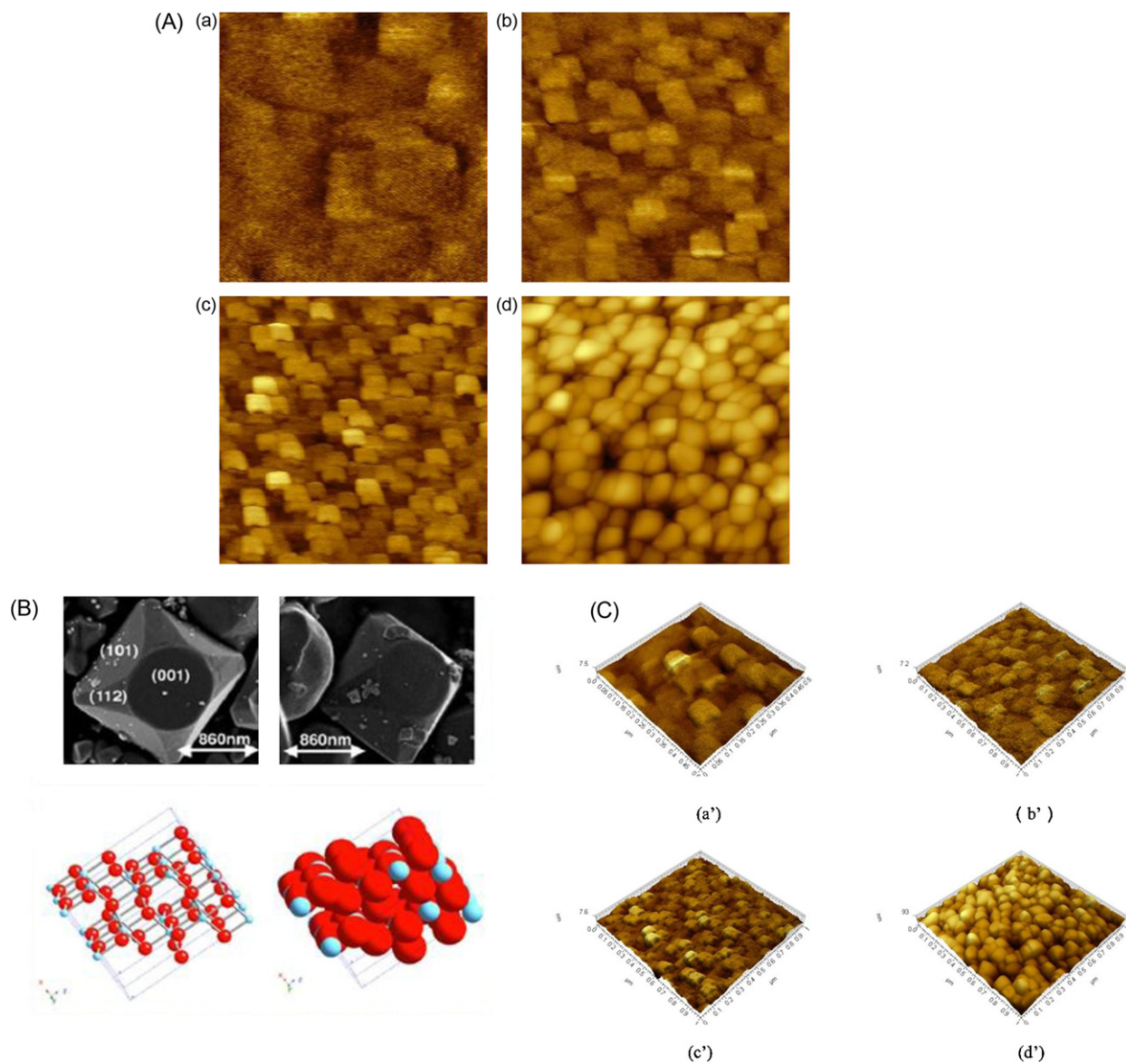


Fig. 5.4. (A) 2D AFM topographical images of anatase phase (a) $x=0$ at%; $y=6$ at%, (b) $x=2$ at%; $y=6$ at%, (c) $x=4$ at%; $y=6$ at%, (d) $x=6$ at%; $y=6$ at% films, and the scanning area was $0.5 \mu\text{m}$, $1 \mu\text{m}$, $1 \mu\text{m}$, $1 \mu\text{m}$, respectively. (B) (a) the SEM image of an anatase particle, (b) an anatase particle after sequential UV irradiation in the same solution as in (a) and then in an aqueous solution of $0.1 \text{ M Pb}(\text{NO}_3)_2$ [48], respectively. ©2003. The Royal Society of Chemistry and the Center National de la Recherche Scientifique. (C) Schematic representations of selected low-index (101) face of anatase. (C) (a')–(d') were the 3D images that corresponding to the (a)–(d).

Table 3

Absorption edge (nm), E_g^a , surface elemental quantity^b (at%) determined from XPS data of all the samples.

Sample	Absorption edge (nm)	E_g^a	Surface elemental quantity ^b (at%)			
			Ti	O	V	N
TiO ₂	385	3.22 eV	32.1	67.9	–	–
Ti _{0.98} V _{0.02} O ₂	403	3.07 eV	31.9	66.2	1.91	–
Ti _{0.96} V _{0.04} O ₂	415	2.98 eV	31.8	64.3	3.90	–
Ti _{0.94} V _{0.06} O ₂	475	2.61 eV	30.4	63.8	5.85	–
TiO _{1.94} N _{0.06}	425	2.92 eV	32.1	62.0	–	5.91
Ti _{0.98} V _{0.02} O _{1.94} N _{0.06}	440	2.82 eV	31.3	60.7	1.95	5.95
Ti _{0.96} V _{0.04} O _{1.94} N _{0.06}	466	2.66 eV	29.4	60.8	3.96	5.92
Ti _{0.94} V _{0.06} O _{1.94} N _{0.06}	496	2.50 eV	27.4	60.6	5.89	5.96

^a Band gap energy, calculated using the transformed *Kubelka–Munk* function.

^b Surface elemental quantity (at%), Results of curve fitting of the XPS spectra for the Ti2p, O1s, V2p, N1s regions.

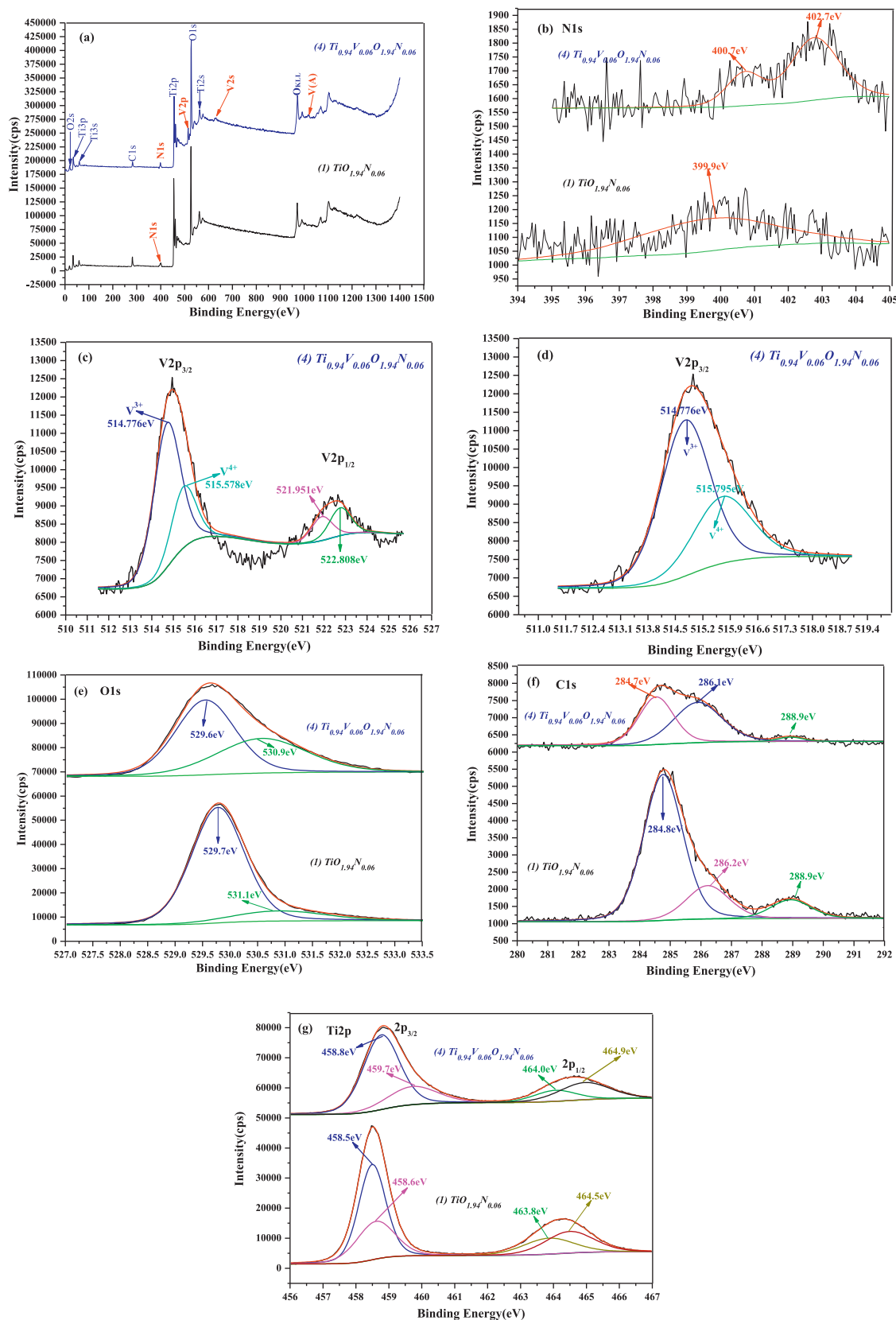


Fig. 5.5. The XPS spectra (after Charge calibration) for post heat treated films (1) and (4) with $x=0$ at%, 6 at%; $y=6$ at% doping concentration, respectively. (a) Full spectra of (1) and (4), the anticipative N and V peak were arising. (b) N1s peak after fitting, the B.E. (eV) shift to higher location (ca. 400.2 eV of N-TiO₂ and 402.6 eV of V-N-TiO₂ compared to nitrogen elementary substance 397.2 eV, respectively). (c) V2p_{3/2} and V2p_{1/2} peak location and the percentage of V³⁺ at 514.7 eV and V⁴⁺ at 515.8 eV, (d) V2p_{3/2} region of N-V-TiO₂ alone, the V³⁺ and V⁴⁺ ratio was equal to the peak in graph (c). (e) O1s peaks which were ascribed to different O source. (f) C1s peaks were separate into three types. (g) Ti2p different percentage of various valence states.

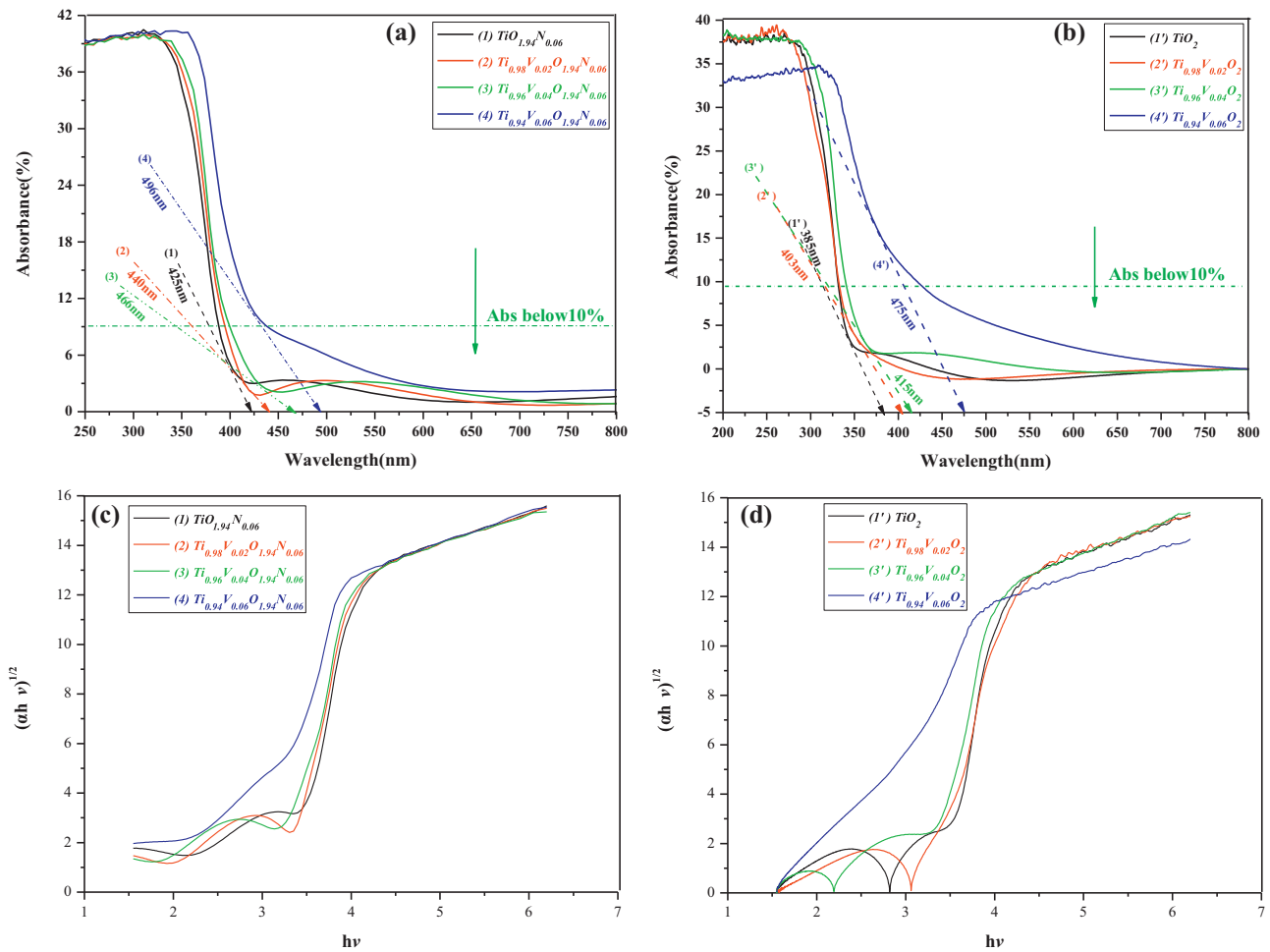


Fig. 5.6. The UV-vis absorption spectra of all type of doping concentration samples (a) N mono-doped and V/N co-doped TiO₂ films, (b) pure and V mono-doped TiO₂ films. (c), (d) are the $(\alpha h\nu)^{1/m} \sim h\nu$ relationships of serial films.

5.2.4. The optical properties of film

Fig. 5.6(a) and (b) shows the UV-vis absorption spectra of all type of doping concentration films which undergo the same annealing program. In graph (a), it is clear that (I) all the V/N co-doped films have a larger absorption edge (i.e. the red-shift edge) compared to N mono-doped one, and a larger extent of shifting corresponds to the doping concentration regularly. The increment of (1)–(3) approximately 20–25 nm, while the (4) (ca.478 nm) has a larger increment as compared with the first three samples, conjecturing that $\text{Ti}_{0.94}\text{V}_{0.06}\text{O}_{1.94}\text{N}_{0.06}$ possesses a better photo response ability that closely linked with the yield rate and quantity of h^+/e^- pairs, which will affects photo-catalytic photo-hydrophilicity further. (II) The absorption edge of films, when $x \geq 4$ at%, extending to the visible light region, means it can be excited by VL to varying degrees. (III) The doped films were all have an enhanced absorption and existed absorption shoulder in visible light region compared to pure TiO₂ film. There is also a significant enhancement when the concentration of doped V increases to 6 at%. The above two phenomena are all attributed to the transition electron from the localized impurity band to the CB. (IV) the existence of V may avail to decrease the energy barrier for nitridation, therefore, the (4) film optical property which reflected by the absorption is superior to the other.

It can be seen from the graph (a) and (b) that the optical properties of (1) and (3') film possess the similar performances, it may draw a conclusion that mono-doped concentration nitrogen (6 at%) and vanadium (4 at%) form the similar impurity band in the gap,

while these levels were induced near the top of VB (O2p) and below the bottom of CB (Ti3d) by N and V, respectively. Acting as trapping centers for electron–hole pairs and then the photo responsibility is enhanced. The similar situation also existed between (3) and (4'),

According to the UV-vis spectra of samples, absorption coefficient α can be estimated by the following Eq. (5-4a):

$$T = e^{-\alpha \cdot d} \quad (5-4a)$$

where T is the transmittance of samples, and d is thickness value of films. The band-gap values of $\text{Ti}_{1-x}\text{V}_x\text{O}_{2-y}\text{N}_y$ film samples can be estimated by the following Eqs. (5-4b) and (5-4c):

$$\alpha = \frac{c}{h\nu} (h\nu - E_g)^m \quad (5-4b)$$

$$E_g = h\nu - \frac{\alpha h\nu}{c} \quad (5-4c)$$

where c is constant and $h\nu$ represents the energy of photon; α is absorption coefficient. $m = 1$ and $1/2$ for indirect and direct semiconductor, respectively. E_g can be estimated by intersecting point value of relationship curve (between $(\alpha h\nu)^{1/m}$ and $h\nu$) and horizontal ordinate ($h\nu$) [22,43] (see Fig. 5.6c and d). E_g values of $\text{Ti}_{1-x}\text{V}_x\text{O}_{2-y}\text{N}_y$ with various x and y are listed in Table 3.

The values of E_g that were calculated by the above equation present an obvious tendency that the band gap reduced along with the V-doped increasing concentration. The minimum one was 2.50 eV (see Table 3), means that it was easily excited by the waves of visible light region which has a lower energy than ultraviolet

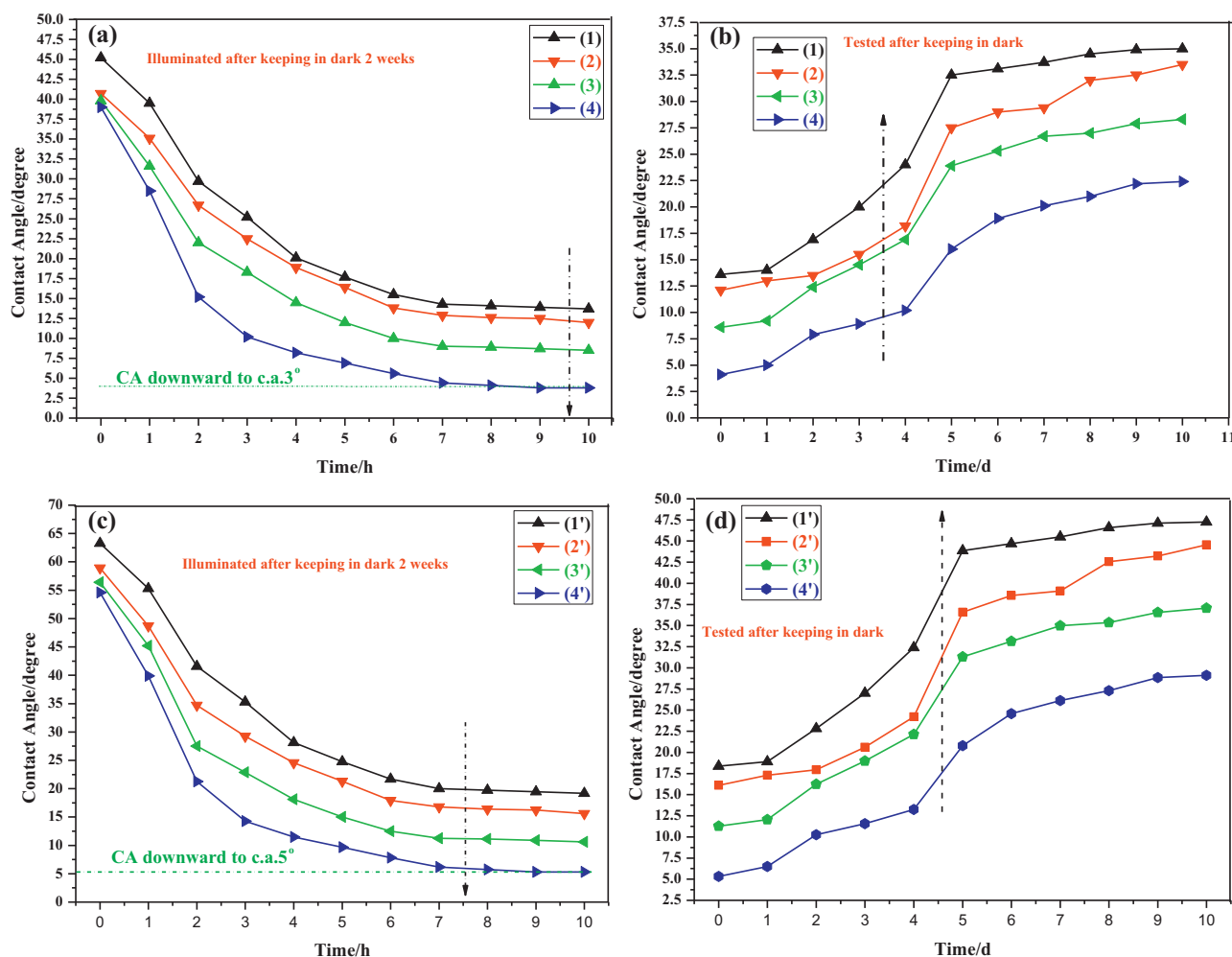


Fig. 5.7. The surface contact angle change of all type films: $\text{Ti}_{1-x}\text{V}_x\text{O}_{2-y}\text{N}_y$ ($x=0\text{ at\%}$, 2 at\% , 4 at\% , 6 at\% ; $y=0\text{ at\%}$, 6 at\%) doping concentration, respectively, illuminating condition: light wavelength $\lambda > 420\text{ nm}$ and intensity 3 mW/cm^2 . (a) and (c) show the reduction of CA under visible light with different illumination time, (b) and (d) which rebound to a large one with varying degrees while kept in dark.

light. It was also confirmed by the calculations of first principles method in Sections 2 and 4.

The computer simulation results in Section 2 (the DOS figure) shows that the 3d state of V has already connected with the conduction band of Ti, which leads to the increment of CB (degenerate energy level) and then the gap band decreases from 3.2 eV to 2.50 eV. The 3d state of V has been separated into two parts by the Fermi energy that located at 0 eV, which indicates that TiO_2 has become a ground state of half metal after the V atoms doping.

5.2.5. Photo hydrophilicity of film surface

Fig. 5.7. Shows the changes of surface CA vs. illumination time of all type films. All the films were stored in dark place for 2 weeks before the first CA was measured, Fig. 5.7(a) and (c) reveal that the starting surface CA was avg. 45° , indicating (indicating) that films have relatively good hydrophilicity, as the light (3 mW/cm^2) irradiation time extending, CA that was checked every hour on the different films' surface descended gradually. CA approached to a constant value which ranging from 5° to 15° after 8–9 h, revealing that the surface state becomes hydrophilic. This might be ascribed to factors such as decreased crystal grain size and narrowed band gap which is affected by the doped concentration. On the one hand, we can conclude that there are more kinds of active groups exist on the higher dopant concentration films surface than a lower one, on account of the incorporation of N and V to TiO_2 lattice leading

to a restrict of grain growth. On the other hand, as discussed in Section 5.2.4, N/V-incorporation narrows the film band gap, thus electrons–holes pairs can be activated easier than pure one by visible light. In addition, the recombination of electron–hole pairs was restrained by these dopants for it acts a role of trapping center. Therefore, the free charge carriers can move to the surface, holes react with lattice oxygen, leading to the formation of surface oxygen vacancies, which contributes to the absorption in the visible light region. While the formation of oxygen vacancies was facilitated by the doped nitrogen due to the presence of doped nitrogen reduce the formation energy of oxygen vacancies [50]. Other radicals, $\cdot\text{OH}$, $\text{O}_2\cdot^-$ and O^- , are also produced by the increased free holes and electrons with molecule oxygen or adsorbed water on surface, and then leads to a series of complex reactions (reactions were listed in Section 5.2.6.) which enhance the hydrophilicity.

Fig. 5.7(b) and (d) shows that CA changes when stored in dark, there is a slow increment in the first four days, indicates the film has a good hydrophilicity to keep capacity. The increment rate of CA reaches to a maximum value when kept in dark between 4th and 5th day. And then, the curve alters to a slightly increasing tendency again. The final measured values are close to a constant that slightly less or more than the initial value exhibited in graph (a) and (c), respectively. The possible reason was that the defective sites (Ti^{4+} or V^{4+} to its lower element valence Ti^{3+} or V^{3+}) that were engendered by surface trapped e^- were sealed up, and the reaction between

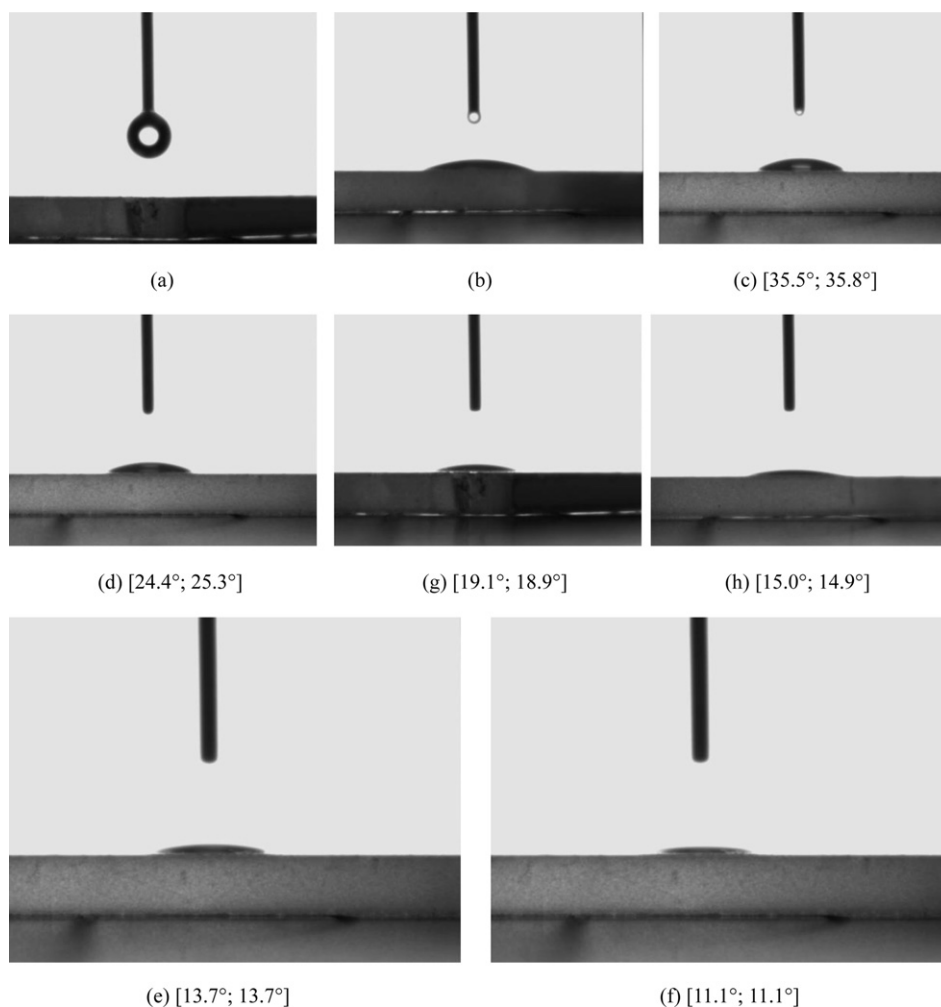


Fig. 5.8. Surface contact angle changes of 2nd film (graph c–f) vs. visible light irradiation time. For instance (c) [35.5°; 35.8°], the two numbers signify the left and right angle water droplet, respectively.

h^+ and the surface adsorbed water was ceased, then the number of functional hydroxyl radicals that triggered by h^+ in the VB original location, which tends to hold back the photo induced (inducing) hydrophilicity (Fig. 5.8).

5.2.6. Evaluation of photo-catalytic properties

The photo-catalytic activities of N and V mono-, V/N co-doped TiO_2 films are evaluated by monitoring the degradation of RhB under visible light. UV–vis absorbance spectra of RhB obtained with (4) film under different illumination times exhibited with Fig. 5.9a, Rhodamine B shows a major absorption band at 551 nm, Visible light irradiation ($\lambda > 420$ nm) of the aqueous RhB/V–N– TiO_2 dispersion leads to an apparent decrease in absorption with a concomitant wavelength shift of the band to shorter wavelengths (Fig. 5.9a), this shift is attributed to N-de-alkylation process, as revealed by MALDI-TOF and liquid chromatography/mass spectral techniques (LC–MS) [52]. The model contaminant can be finally degraded to 6% remnant approximately. The absorbance is then converted to the concentration (C_t) compared to initial (C_0) in Fig. 5.9b shows that the photo-catalytic decomposition efficiency of (1)–(4) TiO_2 films under visible light, confirming to the UV–vis spectra in Fig. 5.6 that the V/N co-doped films' ability are much higher than that of N– TiO_2 film. The kinetics of RhB decomposition appears to be pseudo-zero-order initially with respect to the C/C_0 of model pollutant decomposed. This result is consistent with the result reported by Gu and co-workers [18]. Optimum doping concentration was

obtained from V/N co-doped (4) TiO_2 film, which degrades RhB with a rate constant $7.7 \times 10^{-3} \text{ mol L}^{-1} \text{ min}^{-1}$, which approximate 4 and 9 times higher than that of N– TiO_2 ($1.94 \times 10^{-3} \text{ mol L}^{-1} \text{ min}^{-1}$) and pure TiO_2 films ($0.8 \times 10^{-3} \text{ mol L}^{-1} \text{ min}^{-1}$), respectively. For the V/N co-doped TiO_2 films, it is suggested that the enhanced photo-catalytic activities under visible light are mainly attributed to the synergetic effect between doped N and V atoms. There is also a type of carbon element affects the film property, which exists in the film inherently, It has been reported that the carbon acted as a photo-sensitizer, which could be excited to injecting electrons into the conduction bands of TiO_2 [49]. Then, the electrons could be transferred to the surface-adsorbed oxygen molecules and form superoxide anions, which could further transformed to $\cdot OH$ or $\cdot O_2^-$ radical and initiate the degradation of RhB within 100 ns, and this oxidation pathway is sometimes designated as indirect oxidation, in comparison to the direct oxidation by holes [48]. The doped N atoms improve the visible light absorption, while the doped V atoms can facilitate the formation of oxygen vacancies, which are generally regarded as an important active species to ignite the formation of oxygen vacancies, which are generally regarded as an important active species for initiating a photocatalytic reaction. Fig. 5.9c shows the reaction rate constant k of (4) film, is Avg. $7.4 \times 10^{-3} \text{ mol L}^{-1} \text{ min}^{-1}$, Fig. 5.9d shows the reaction rate constant k of (1)–(4), and presents a linear relation, which correspond to too many former researchers' conclusions.

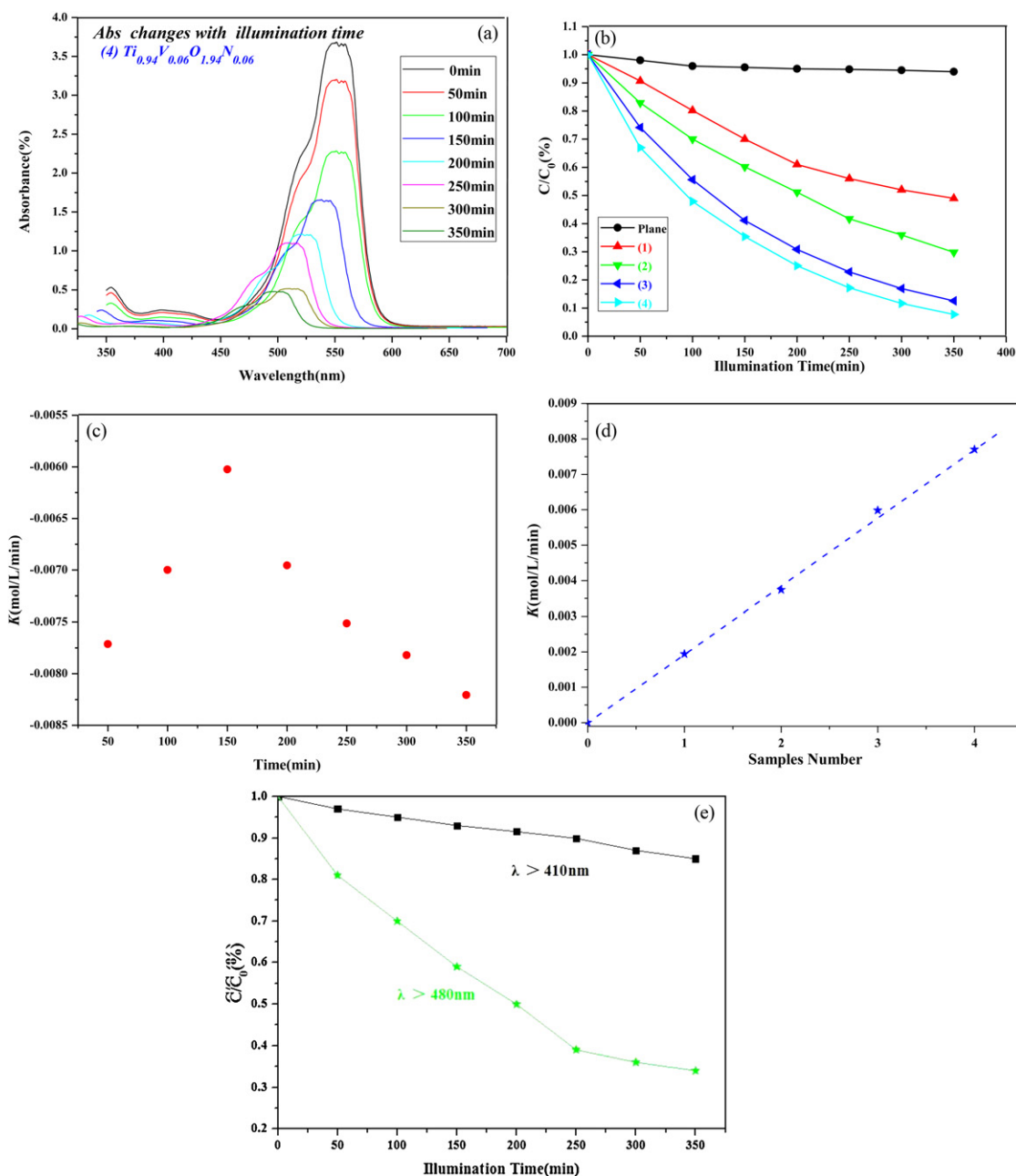


Fig. 5.9. Time dependence of model pollutant RhB concentration during photo degradation of all type films deposited on quartz glass under visible light, initial RhB concentration was 0.012 mM. (a) RhB absorbance spectrum at 551 nm of (4) sample, (b) comparison of the RhB photo degradation extent of plane substrates and (1)–(4) film, (c) the reaction rate constant k of (4), Avg. $7.4 \times 10^{-3} \text{ mol L}^{-1} \text{ min}^{-1}$, fluctuation range was from $8.21 \times 10^{-3} \text{ mol L}^{-1} \text{ min}^{-1}$ to $6.02 \times 10^{-3} \text{ mol L}^{-1} \text{ min}^{-1}$. (d) The reaction rate constant k of (1)–(4), which presents a linear relation. (e) Photocatalytic degradation of RhB over $\text{Ti}_{0.94}\text{V}_{0.06}\text{O}_{1.94}\text{N}_{0.06}$ film under different irradiation lights, pH 7.20.

It is well known that ion doping usually introduces impurity energy levels within the energy band gap, which help to enhance the visible-light absorption owing to the reduced band gap. Doping with anions leads to impurity levels above the valence band, while transition metal cation leads to impurity levels under the conduction band. The impurity levels can locate shallowly or deep in the band gap depends on dopant and the number of impurity band that depends on the dopant concentration. A shallow impurity level tends to perform as a trapping center and enhance the photocatalytic activity, while a deep one usually acts as a recombination center and leads to a decrease of the photo-catalytic activity of TiO_2 . In the present test, the photo-catalytic activity of all films was enhanced, indicating that the dopant in this work below the optimal concentration limit, acting as a role of trapping center rather than a

recombination center. N species and V ions act as the hole-trapping sites and electron-trapping ones, respectively.

Considering the potential of V ions more positive ($E_{\text{V}_{\text{ads}}^{4+}/\text{V}_{\text{ads}}^{3+}} = 0.337 \text{ V}$) than the CB ($E_{\text{cb}} = -0.5 \text{ V}$) and one electron reduction reaction for oxygen molecules ($\text{EO}_2/\text{O}_2^{\bullet-} = -0.33 \text{ V}$), which means the reaction that oxygen molecule trap electron is suppressed, while the fact is that the dye of RhB ($E_{\text{RhB}^{+ \bullet}/\text{RhB}} = -1.09 \text{ V}$) is photo-degraded with the color changing phenomena. Therefore, the photo-degradation of RhB might be through the two concomitant reactions.

On the one hand, it has been found that the $\bullet\text{OH}$ radicals are generated in the two-doping system during the pollutant photo-degradation. In this system, incorporation of N into TiO_2 can extend the spectral response to the visible region owing to the reduced

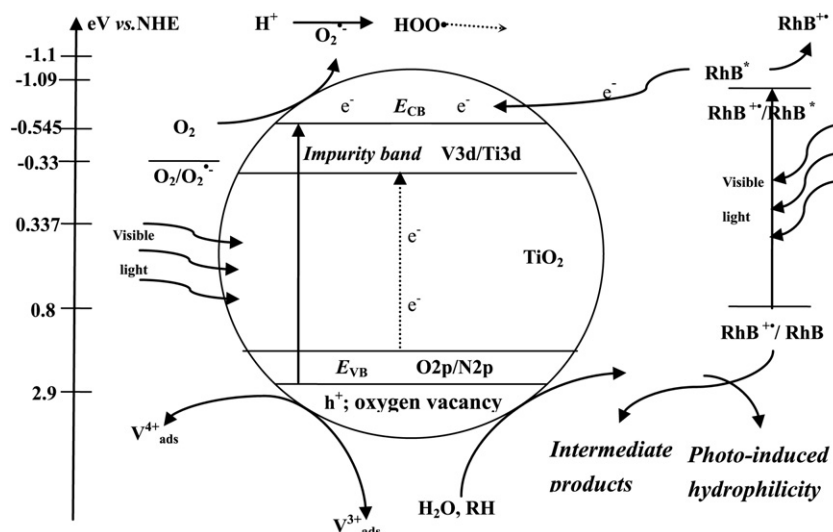
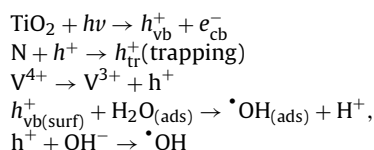


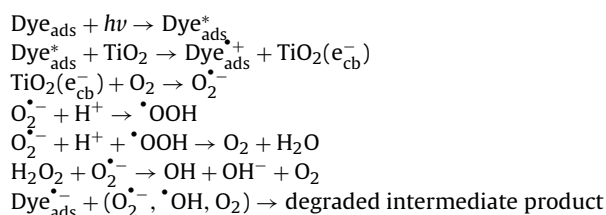
Fig. 5.10. The scheme of the proposed mechanism of the photo-degradation of RhB and photo-hydrophilicity on V/N-TiO₂ films under visible light irradiation.

band gap and function as an antenna, and the further loading of V into the matrix can suppress the charge recombination and enhance greatly the photocatalytic activity. Thus, photosensitized degradation of dyes does involve VB hole in photochemical process, mineralization of dyes finds its origins with the active oxygen radical species ($O_2^{\bullet-}$), and the radical cations. The reaction possibly includes the following process:



On the other hand, in this study, V/N-TiO₂ also shows the photo reaction when the wavelength much longer than 470 nm. About 15% of RhB is photo-degraded after ca. 6 h of irradiation ($\lambda > 480$ nm), as shown in Fig. 5.9e. It is well-known that RhB can absorb the visible light in the range 460–600 nm, which is attributed to the ground state and the excited state of the dye. Thus, the materials absorbing light irradiation should be RhB and V/N-TiO₂ together in the experiment. Among these, RhB is the main material absorbing light irradiation when $\lambda > 470$ nm. The RhB photo degradation is attributed to the photosensitized mechanism when $\lambda > 470$ nm, namely, the RhB dye first absorb the incident photon. Then, the photo-generated electrons are transferred to the excited state of the dye by the intra-molecular radical transition and the dyes are oxidized. The photoelectrons of the excited state are immediately injected into the CB (V_{3d}/Ti_{3d} level) of V/N-TiO₂. The photoelectrons in the CB are then captured by O_2 , and the subsequent recycle reactions lead to the mineralization of the dyes. The scheme of the proposed photosensitized pathway mechanism of the RhB photo-degradation on V/N-TiO₂ films under visible light irradiation is shown in Fig. 5.10. This process might be similar to the surface sensitization of TiO₂ via adsorbed dyes.

The proposed photosensitized mechanism:



Due to the mean lifetime of photo-generated pairs is prolonged. The opportunity that the electron–hole pairs in the co-doped systems move to the surface before recombination is increased. The photosensitization process involves initial excitation of the dye molecules, after the electron is injected from the excited dye into the TiO₂ conduction band, the dye is converted to its cationic radical, the injected electron on the conduction band can reduce surface-sorbed oxidants, usually the molecular oxygen, to yield the oxidizing species such as H_2O_2 , $O_2^{\bullet-}/\cdot\text{OOH}$, and $\cdot\text{OH}$ radicals, which are presumed to be responsible for the dye degradation.

6. Conclusions

In summary, a series of visible-light driven (N and V doped TiO₂: $Ti_{1-x}V_xO_{2-y}N_y$) self-cleaning thin colorful films, which show practically self-cleaning property, were successfully prepared by sol-gel method based on the first principle method density functional theory (DFT). The localized impurity bands, which are attributed to V and N, are apparently arising when the V concentration is 6 at% coupled with 6 at%N. The film that was doped with $x=6$ at%, $y=6$ at% possesses the optimal photo properties, indicating that the critical (up-limit) vanadium doping quantity derived from the residual quantity of lattice binding energy was credible. Then, the surface structures and properties analysis of all the type films also manifest that the $Ti_{0.94}V_{0.06}O_{1.94}N_{0.06}$ film possesses the best photo responsibility than other composition, which verifies the result of CASTEP5.0 calculation. We can infer that the up-limit V doping quantity might be ca.6 at%, the V/N co-doping might has a synergetic effect and mutual promoted relations to enhance the photo-catalytic activity and hydrophilicity. The current simple approach of coating doped TiO₂ onto glass substrates could potentially be applied to other substrates for the preparation of colorful and transparent doped TiO₂ surface coating for self-cleaning and other applications.

References

- [1] A. Fujishima, X.T. Zhang, D.A. Tryk, Surface Science Reports 63 (2008) 515–582.
- [2] A. Fujishima, K. Honda, Nature 238 (1972) 37–39.
- [3] R. Wang, K. Hashimoto, A. Fujishima, et al., Nature 338 (1997) 431–432.
- [4] R. Wang, K. Hashimoto, A. Fujishima, et al., Advanced Materials 10 (1998) 135.
- [5] N. Sakai, R. Wang, A. Fujishima, et al., Langmuir 14 (1998) 5918.
- [6] T. Watanabe, A. Nakajima, R. Wang, et al., Thin Solid Films 351 (1999) 260.
- [7] R. Asahi, T. Morikawa, T. Ohwaki, et al., Science 293 (2001) 269–271.

- [8] A. Borrás, C. Lopez, V. Rico, et al., *Journal of Physical Chemistry C* 111 (2007) 1801–1808.
- [9] J.C. Yu, J. Yu, W. Ho, et al., *Chemistry of Materials* 14 (2002) 3808–3816.
- [10] G. Liu, Y. Zhao, C. Sun, et al., *Angewandte Chemie International Edition* 47 (2008) 4516–4516.
- [11] Di.C. Valentin, E. Finazzi, G. Pacchioni, *Chemistry of Materials* 20 (2008) 3706–3714.
- [12] Q.C. Xu, D.V. Wellia, M.A. Sk, et al., *Journal of Photochemistry and Photobiology A: Chemistry* 210 (2010) 181–187.
- [13] Y.C. Lee, Y.P. Hong, H.Y. Lee, et al., *Journal of Colloid and Interface Science* 267 (2003) 127–131.
- [14] J.G. Yu, M.H. Zhou, H.G. Yu, et al., *Materials Chemistry and Physics* 95 (2006) 193–196.
- [15] R. Subasri, M. Tripathi, K. Murugan, et al., *Materials Chemistry and Physics* 124 (2010) 63–68.
- [16] L. Li, C.Y. Liu, Y. Liu, *Materials Chemistry and Physics* 113 (2009) 551–557.
- [17] S.M. Chang, W.S. Liu, *Applied Catalysis B: Environmental* 101 (2011) 333–342.
- [18] D.E. Gu, B.C. Yang, Y.D. Hu, *Catalysis Communications* 9 (2008) 1472–1476.
- [19] M. Miyauchi, *Journal of Materials Chemistry* 18 (2008) 1858–1864.
- [20] S.A.K. Leghari, S. Sajjad, F. Chen, et al., *Chemical Engineering Journal* 166 (2011) 906–915.
- [21] T. Tatsuma, S. Takeda, S. Saitoh, et al., *Electrochemistry Communications* 5 (2003) 793–796.
- [22] H. Li, G.L. Zhao, G.R. Han, et al., *Surface and Coatings Technology* 201 (2007) 7615–7618.
- [23] P.G. Wu, R.C. Xie, J.A. Imlay, et al., *Applied Catalysis B: Environmental* 88 (2009) 576–581.
- [24] M. Houmard, D. Riassetto, F. Roussel, et al., *Surface Science* 602 (2008) 3364–3374.
- [25] S. Permpoon, M. Houmard, D. Riassetto, et al., *Thin Solid Films* 516 (2008) 957–966.
- [26] W.C. Chien, Y.Y. Yu, P.K. Chen, et al., *Thin Solid Films* 519 (2011) 5274–5279.
- [27] T. Jiang, L. Miao, S. Tanemura, et al., *Microstructure* 46 (2009) 159–165.
- [28] M. Takeuchi, Y. Onozaki, Y. Matsumura, et al., *Nuclear Instruments and Methods in Physical Research Section B* 206 (2003) 259–263.
- [29] R. Cai, G.M. Van, P.K. Aw, et al., *Comptes Rendus Chimie* 9 (2006) 829–835.
- [30] Z.L. Shi, C. Du, S.H. Yao, *Journal of Taiwan Institute of Chemical Engineering* 42 (2011) 652–657.
- [31] J. Domaradzki, D. Kaczmarek, A. Borkowska, et al., *Vacuum* 82 (2008) 1007–1012.
- [32] X. Chen, P. Glansb, *Journal of Electron Spectroscopy and Related Phenomena* 162 (2008) 67–73.
- [33] S. Karvinen, P. Hirva, T.A. Pakkanen, *Journal of Molecular Structure: THEOCHEM* 626 (2003) 271–277.
- [34] Z.B. Zhang, C.C. Wang, R. Zakaria, et al., *Journal of Physical Chemistry B* 102 (1998) 10871.
- [35] A. Mills, A. Lepre, N. Elliott, et al., *Journal of Photochemistry and Photobiology A: Chemistry* 160 (2003) 213–224.
- [36] B.H. Kim, J.Y. Lee, Y.H. Choa, et al., *Materials Science and Engineering B107* (2004) 289–294.
- [37] F.M. Meng, X.P. Song, Z.Q. Sun, et al., *Vacuum* 83 (2009) 1147–1151.
- [38] M. Terashimaa, N. Inouea, S. Kashiwabaraa, *Applied Surface Science* 169–170 (2001) 535–538.
- [39] D.G. Huang, S.J. Liao, J.M. Liu, et al., *Journal of Photochemistry and Photobiology A* 184 (2006) 282–288.
- [40] M.C. Payne, M.P. Teter, D.C. Ahan, *Review Modern Physics* 64 (1992) 1045.
- [41] S.J. Clark, M.D. Segall, P.J.D. Lindan, et al., *Journal of Physics* 220 (2005) 567.
- [42] X.G. Qu, W.X. Liu, W.B. Cao, et al., *Materials Science Forum* 622 (2009) 703–706.
- [43] H.L. Liu, Z.H. Lu, L. Yue, et al., *Applied Surface Science* 257 (2011) 9355–9361.
- [44] J.P. Perdew, K. Burke, M. Ernzerhof, *Physical Review Letters* 77 (1997) 3865–3868.
- [45] M. Kitano, K. Funatsu, M. Matsuoka, et al., *Journal of Physical Chemistry B* 110 (2006) 25266–25272.
- [46] Y.J. Chen, *Applied Catalysis B: Environmental* 69 (2006) 24–33.
- [47] O.U. Nimitrakoolchai, S. Supothina, *Journal of the European Ceramic Society* 28 (2008) 947–952.
- [48] T. Taguchi, Y. Saito, K. Sarukawa, et al., *New Journal of Chemistry* 27 (2003) 1304–1306.
- [49] X. Yang, C. Cao, L. Erickson, et al., *Journal of Catalysis* 260 (2008) 128–133.
- [50] A. Fujishima, X. Zhang, D.A. Tryk, *Journal of Surface Science Reports* 63 (2008) 515–582.
- [51] P.H. Wang, P.S. Yap, T.T. Lim, *Journal of Applied Catalysis A: Gene* 399 (2011) 252–261.
- [52] C. Chen, W. Zhao, J. Li, J. Zhao, H. Hidaka, N. Serpone, *Environmental Science & Technology* 36 (2002) 3604.